

# Formation mechanism of nano-sized $\eta$ and $\omega$ structures in $\beta$ phase in ECP treated Cu-40Zn alloy

Meishuai Liu<sup>a,b,c</sup>, Yudong Zhang<sup>c,\*</sup>, Xinli Wang<sup>d</sup>, Benoit Beausir<sup>c</sup>, Xiang Zhao<sup>b,\*</sup>, Liang Zuo<sup>b</sup>, Claude Esling<sup>c</sup>

<sup>a</sup> Research Center of High-temperature Alloy Precision Forming, School of Material Engineering, Shanghai University of Engineering Science, Shanghai 201620, China

<sup>b</sup> Key Laboratory for Anisotropy and Texture of Materials (Ministry of Education), Northeastern University, Shenyang 110819, China

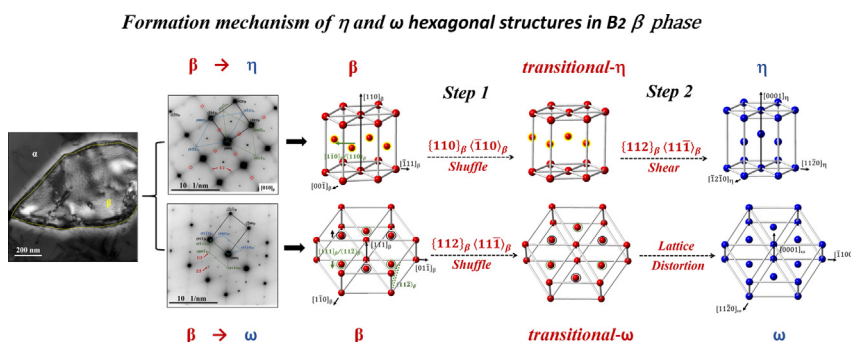
<sup>c</sup> Laboratoire d'Étude des Microstructures et de Mécanique des Matériaux (LEM3), CNRS UMR 7239, Université de Lorraine, Metz 57073, France

<sup>d</sup> Research Institute, Northeastern University, Shenyang 110819, China

## HIGHLIGHTS

- Two kinds of hexagonal structures are identified in the  $\beta$  precipitates of a Cu-40Zn alloy to be formed through a two-stepped atomic displacement.
- The concomitant formation of the two hexagonal structures minimize the lattice distortion of each single formation.
- The new information on the formation mechanism of the two hexagonal structures in a Body Centre Cubic matrix are provided, which is a common feature of many alloys systems.

## GRAPHICAL ABSTRACT



## ARTICLE INFO

### Article history:

Received 9 December 2021

Revised 12 January 2022

Accepted 16 January 2022

Available online 20 January 2022

### Keywords:

Structure transition

Atomic shuffle

Hexagonal structure

Cu-Zn alloy

Deformation gradient tensor

## ABSTRACT

Two nano-scaled hexagonal distortions in high temperature BCC phase during cooling is commonly observed in many alloys systems. Although efforts have been made on studying the lattice softening of the BCC structure during cooling, the distortion mechanisms are less addressed. Thus, the formation of two hexagonal structures in the  $\beta$  precipitates in a Cu-40Zn alloy treated by ECP was thoroughly investigated. Results show that the  $\beta$  precipitates contain two kinds of nano-sized and diffuse atomic clusters one with a  $\eta$  structure obeying the Burgers OR and the other a  $\omega$  structure obeying the Blackburn OR. They were each formed through a two-stepped atomic displacement. For the  $\eta$  structure, the first step is the atomic shuffle of each second  $\{110\}_{\beta}$  plane in the  $\langle 110 \rangle_{\beta}$  direction and the second is a structure change mainly by a  $\{1\bar{1}2\} \langle \bar{1}11 \rangle_{\beta}$  shear. For the  $\omega$  structure, the first is an atomic shuffle on each second and third  $\{11\bar{2}\}_{\beta}$  plane in the  $\pm [111]_{\beta}$  directions and then normal strains in three mutually perpendicular directions. The concomitant formation of the two structures minimizes the lattice distortion of single formation. The present results provide new information on the formation mechanism of the two hexagonal structures in a BCC matrix.

© 2022 The Authors. Published by Elsevier Ltd. This is an open access article under the CC BY-NC-ND license (<http://creativecommons.org/licenses/by-nc-nd/4.0/>).

## 1. Introduction

Characteristic atomic shuffles or displacements on certain shear systems of high temperature BCC phase on quenching has been an intrinsic feature of many alloys systems, such as Ti-based alloys [1–20], Zr-based alloys [1,21] and Cu-based alloys [22–28]. The

\* Corresponding authors.

E-mail addresses: [yudong.zhang@univ-lorraine.fr](mailto:yudong.zhang@univ-lorraine.fr) (Y. Zhang), [zhaox@mail.neu.edu.cn](mailto:zhaox@mail.neu.edu.cn) (X. Zhao).

shuffles commonly result in the formation of two kinds of hexagonal structures in a form of nano-sized atomic clusters. The two structures have often been observed in  $\beta$  quenched Ti alloys and Zr alloys. Of the two hexagonal structures, one possesses a crystal structure close to that of the equilibrium  $\alpha$  phase and obeying the Burgers orientation relation (BOR) with the  $\beta$  matrix [1], and the other have a crystal structure resembling that of the metastable  $\omega$  phase and obeying the Blackburn OR with the  $\beta$  matrix [3]. Due to the two kinds of structure distortions in the  $\beta$  matrix, additional weak reflections are produced at the  $1/2$   $\beta$  reflection positions in the TEM Selected Area Electron Diffraction (SAED) patterns for the former and at the  $1/3$  and  $2/3$   $\beta$  reflection positions for the latter [14,16–18]. Experimental investigations have shown that the atomic shuffles or displacements are on the  $\{110\} <1\bar{1}0>$  and  $\{112\} <11\bar{1}>$  shear systems [18] and the shear moduli of the two systems tend to soften with the drop of the temperature [7]. It has also been revealed that the softening of the two shear systems corresponds to the lower energy or soft phonon modes of the  $\beta$  phase [2,7,21,29].

The lattice instability resulting from the soft phonon modes of the two shear systems is also the inherent feature of the  $B_2$   $\beta$  or  $\beta'$  phase (having an ordered BCC structure) in the Cu-Zn alloys [24,27]. Some electron diffraction phenomena have also been found in the ordered BCC  $\beta$  phase at room temperature [24,25,27]. An  $\omega$  typed structure has been observed in the quenched Cu-Zn alloys [22–24]. The atomic displacements on the  $\{110\} <1\bar{1}0>$  system represented by a 4H (hexagonal) stacking sequence has been found in the ordered  $\beta$  phase in the Cu-Zn alloys during the dezincification process [25–28].

Although the connection between the atomic shuffles on the two soft shear systems of the parent BCC  $\beta$  phase and the formation of the two hexagonal structures has been established, the respective strain paths to form the two structures are not clear. Moreover, the reason for the concomitant formation of the two structures has not yet been elucidated. Thus, as one step forward of the current understanding of the common lattice instability of the BCC  $\beta$  phase, we conducted the present work to uncover the strain paths of the formation of the two structures and to figure out the reason for their concomitance. A Cu-40 %Zn alloy was selected and an Electric Current Pulse (ECP) treatment was performed to induce the  $\alpha$  (FCC phase) to ordered BCC  $\beta$  ( $B_2$  phase) transformation by benefiting the ultra-rapid heating and cooling of the treatment. This treatment allows fine  $\beta$  precipitates to be formed from the  $\alpha$  phase during heating and to be retained to the room temperature, as demonstrated by many studies using Cu-Zn alloys [30–32]. A thorough crystallographic analysis on the nano-scaled hexagonal structures in the  $\beta$  precipitates was carried out by the high-resolution scanning transmission electron microscopy (STEM) with an aim to reveal the formation mechanisms of the two hexagonal structures.

## 2. Experimental details

The initial material used in this work is a hot-rolled Cu-40 %Zn alloy sheet ( $300 \times 150 \times 1.5$  mm). The composition measured by the X Ray Fluorescence is given in Table 1.

Dog-bone shaped samples with gauge dimensions of 10 mm in length, 2 mm in width, and 1.5 mm in thickness were cut out of the

**Table 1**  
Chemical composition (in wt. / %) of the hot-rolled Cu-40 %Zn alloy.

Cu%	Zn%	Si%
60.86	39.06	<0.01

center part of the hot-rolled Cu-40 %Zn alloy and then heat treated at 773 K in the  $\alpha + \beta$  phase region for 30 min and cooled in air. The heat-treated samples were further treated by electric current pulse (ECP) treatment at room temperature. The ECP treatment layout is displayed in Fig. 1 (a) [33]. The two ends of each sample were clamped between the copper electrodes under the atmospheric condition. A single electric current pulse was produced by a discharge of the capacitor banks and went through the sample. A typical wave profile of a measured electric current pulse is shown in Fig. 1 (b). The pulse takes a form of a damped oscillation wave. During the treatment, the current density and the pulse duration were instantaneously recorded using a Rogowski coil and a TDS3012 digital storage oscilloscope (Tektronix, Beaverton, Oregon). In the present work, the peak value of the electric current density is 15.93 kA/mm<sup>2</sup> with a duration of 125  $\mu$ s.

The microstructural examinations were performed in a field emission gun scanning electron microscope (SEM, Jeol JSM 6500F) operated at an accelerating voltage of 15 kV and equipped with an EBSD acquisition camera and the Aztec online acquisition software package (Oxford Instruments). During the EBSD measurements, the “beam-control” mode was applied with a step size of 0.15  $\mu$ m. The EBSD data were analyzed with the ATEX software package [34]. The EBSD measurement samples were first mechanically ground using the emery/SiC grinding papers ranging from 1200 grit to 4000 grit (5  $\mu$ m) sizes and then polished using diamond paste (1  $\mu$ m) and finally electrolytically polished at room temperature with a solution of 20 % nitric acid (in volume) in methanol at 18 V for 3 s.

The nano-scaled microstructural and crystallographic features of the constituent phases were analyzed using a Philips CM 200 transmission electron microscope (TEM) operated at 200 kV. The TEM is equipped with a LaB6 cathode, a GatanOrius 833 CCD camera, and the homemade automatic orientation analysis software - Euclid's Phantasies (EP) [35,36]. The atomic scaled microstructural examinations were carried out by high-resolution scanning transmission electron microscopy (STEM), using a JEOL JEM-ARM 200F TEM. High-angular dark-field (HAADF) images were acquired with an inner and an outer collecting angle of 68 and 280 mrad, respectively. TEM thin films were prepared first by mechanical thinning to 80  $\mu$ m and then by electrolytic polishing to perforation at  $-34$  °C with the solution of 20% nitric acid (in volume) in methanol at a voltage of 18 V, using a Struers Tenupol-5 twin-jet electropolisher.

The single-crystal TEM electron diffraction and the atomic correspondences of the structures were simulated using the Crystal Maker software package [37] and the transformation lattice strains were represented with the deformation gradient tensor [38].

## 3. Results and discussion

### 3.1. Microstructural characteristics

Fig. 2 (a) and (b) show the EBSD micrographs of the annealed Cu-40 %Zn alloy before and after the ECP treatment, where the  $\beta$  phase is in red and the  $\alpha$  phase in gray (EBSD band quality indexed contrast). It is seen from Fig. 2 (a) that the annealed microstructure is mainly composed of  $\alpha$  phase with a slight amount of block shaped  $\beta$  phase that was formed during the solidification process. After the ECP treatment, numerous fine  $\beta$  precipitates with bar shape appear in the  $\alpha$  grains, as shown in Fig. 2 (b). Next, we will focus only on the  $\beta$  precipitates induced by the ECP treatment.

Fig. 3 shows a TEM bright-field micrograph of an example  $\beta$  precipitate in the ECPed sample, as marked with the yellow dotted line. The TEM diffraction contrast reveals the existence of fine

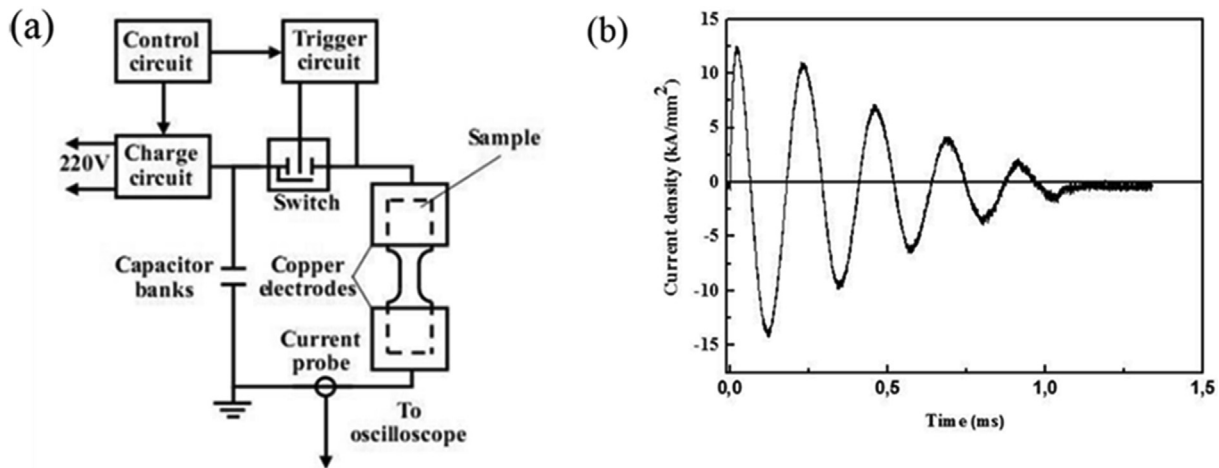


Fig. 1. (a) Illustration of ECP experimental arrangement. (b) A typical waveform of ECP.

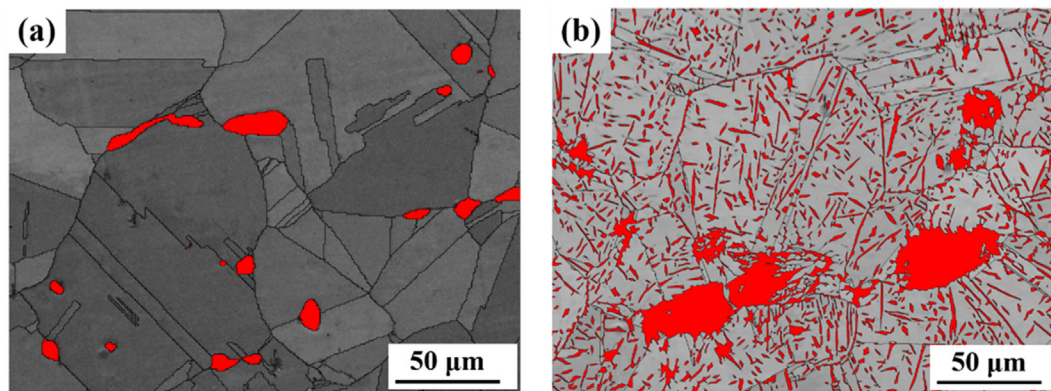


Fig. 2. SEM-EBSD micrographs of the annealed Cu-40 %Zn alloy before (a) and after (b) the ECP treatment, where the  $\beta$  phase is in red and the  $\alpha$  phase is in gray in function of the EBSD band quality indices. (For interpretation of the references to colour in this figure legend, the reader is referred to the web version of this article.)

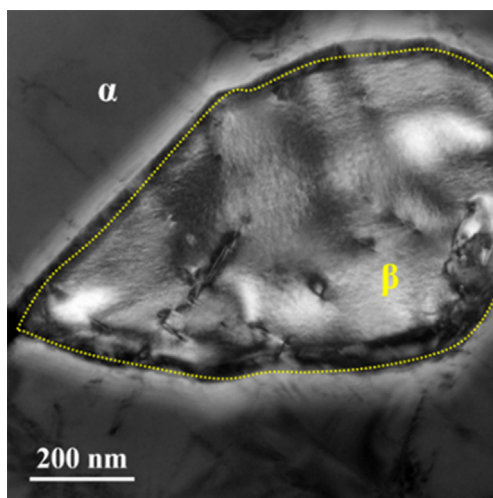


Fig. 3. TEM bright-field micrograph of a  $\beta$  precipitate in the ECPed Cu-40 %Zn sample.

and differently oriented striations that are homogeneously distributed throughout the  $\beta$  precipitates. This suggests that fine substructures exist in the  $\beta$  precipitates.

### 3.2. Identification of substructures in $\beta$ precipitates

Fig. 4 (a) shows a typical  $[010]_{\beta}$  zone axis TEM Selected Area Electron Diffraction (SAED) pattern of the ECP induced  $\beta$  precipitates. In the  $[010]_{\beta}$  zone axis diffraction pattern (Fig. 4 (a)), two sets of diffraction spots are visible. One is from the high-intensity spots plus the low intensity but sharp super lattice spots, as outlined with the black frame. The other is composed of low intensity and diffuse spots located at the  $1/2\{130\}_{\beta}$  reflection positions, as outlined with the dashed frames. The former is from the  $\beta$  precipitates that possess an ordered BCC structure and is typical for the Cu-Zn alloys. The latter corresponds to the reflections from the  $\eta$  phase -  $(\text{Cu}_2\text{Zn}_{98})$  that is a known phase in the Cu-Zn alloys [24,27] and also corresponds to the HCP  $\alpha$  structure in the Ti and Zr alloys. Hereafter we denote it  $\eta$  structure instead of  $\alpha$  structure to avoid confusion with the FCC  $\alpha$  phase in the Cu-Zn alloy systems. In the  $[010]_{\beta}$  zone axis pattern, two orientation variants of the  $\eta$  structure are visible, as indicated with the blue and green frames. The spots located at the  $1/2\{110\}_{\beta}$  reflection positions marked with the red boxes in Fig. 4 (a) are double reflections from the  $(0\bar{1}11)_{\eta}$  and  $(01\bar{1}1)_{\eta}$  planes of the  $\eta$  structure. The simulated SAED patterns of the two variants are shown in Fig. 4 (b). Further crystallographic examination confirmed that the  $\eta$  structure is related to the  $\beta$  structure with the BOR, i.e.,  $\{110\}_{\beta} // \{0001\}_{\eta}$ ,  $\langle \bar{1}11 \rangle_{\beta} // \langle 11\bar{2}0 \rangle_{\eta}$ . This result shows that the  $\beta$  precipitates are not purely ordered BCC but contain some other nano-scaled structures.



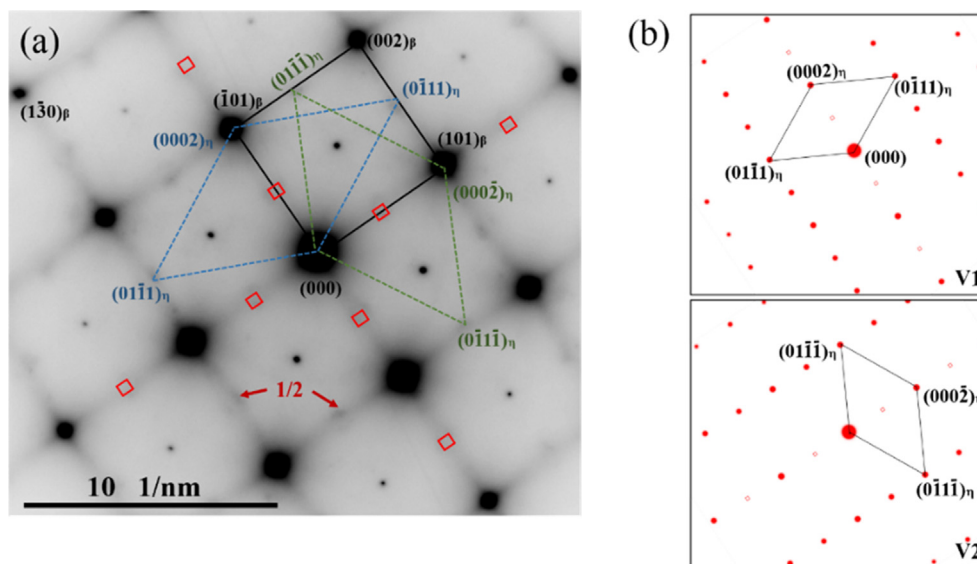


**Fig. 4.** (a) TEM [010]<sub>β</sub> zone axis Selected Area Electron Diffraction (SAED) pattern of the β precipitates in the Cu-40 %Zn sample after the ECP treatment. (b) Simulated SAED patterns using the η structure from two crystallographic orientation variants. Double reflections are marked with the red boxes in (a) and represented with empty squares in (b). (For interpretation of the references to colour in this figure legend, the reader is referred to the web version of this article.)

Fig. 5 shows a typical  $[011]_{\beta}$  zone axis TEM SAED pattern of the ECP induced  $\beta$  precipitates. Two sets of diffraction spots can be clearly observed. The first set is from the high-intensity spots plus the low intensity but sharp super lattice spots from the ordered  $\beta$  structure as outlined with the black frame in the figure. The second set is from the low intensity spots, appearing at the  $1/3$  and  $2/3$   $\{112\}_{\beta}$  reflection positions, as outlined with the dashed frames in Fig. 5 (a). These spots correspond to the reflections from a  $\omega$  structure in the BCC ordered  $\beta$  phase in the Cu-Zn alloys [24]. Such a structure corresponds to that of the  $\sigma$  phase ( $\text{CuZn}_3$ ) that is stable at high temperature. It has a hexagonal structure. Further crystallographic examination confirmed that the  $\omega$  structure is related to the  $\beta$  structure with the Blackburn OR, i.e.,  $\{111\}_{\beta} // \{0001\}_{\omega}$ ,  $\langle \bar{1}1$

$0_{\beta}/\langle 1120 \rangle_{\omega}$ . In the  $[011]_{\beta}$  zone axis SAED pattern, in Fig. 5 (a), there are two sets of  $\omega$  patterns that are from two crystallographic orientation variants, as outlined with the respective blue and green frames in Fig. 5 (a) and the simulated SAED patterns are shown in Fig. 5 (b). This result indicates that in addition to the  $\eta$  structure, the  $\beta$  phase also contains another structure, the  $\omega$  structure. In addition to the two set of diffractions, some faint and diffuse spots appear at the  $1/2\{112\}_{\beta}$  reflection positions, as indicated in Fig. 5 (a). These spots correspond to the reflections from the  $\eta$  structure that has been observed in Fig. 4 (a). It should be noted that the SAED patterns in Fig. 4 (a) and Fig. 5 (a) possess one common feature, i.e., the fine and continuous streaks between the diffraction spots of the two structures passing through the origin (transmitted

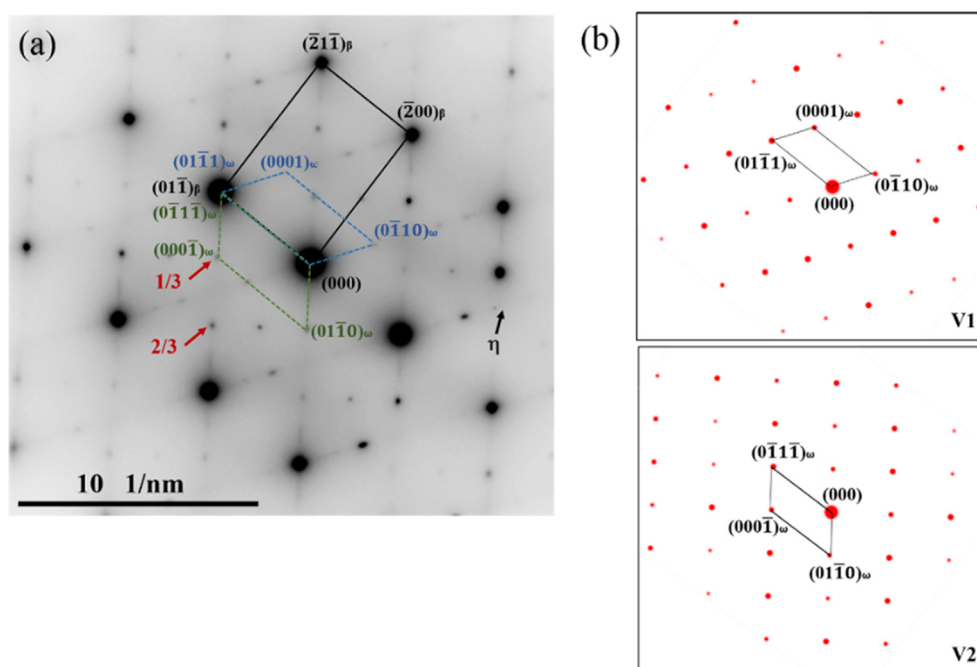


**Fig. 5.** (a) TEM  $[011]_{\beta}$  zone axis SAED pattern of the  $\beta$  precipitates in the Cu-40 %Zn sample after the ECP treatment. (b) Simulated SAED patterns of the two  $\omega$  variants.

beam) of the diffraction pattern. This is the characteristic of the scattering effect arising from crystal size. The fine streaks indicated that the two structures are very small in size. Although the diffraction spots from these structures are visible in the SAED patterns, the dark field micrographs produced using their reflections are very faint and the corresponding structures could not be illuminated. To visualize the atomic arrangements of the two structures, high resolution STEM examinations were conducted.

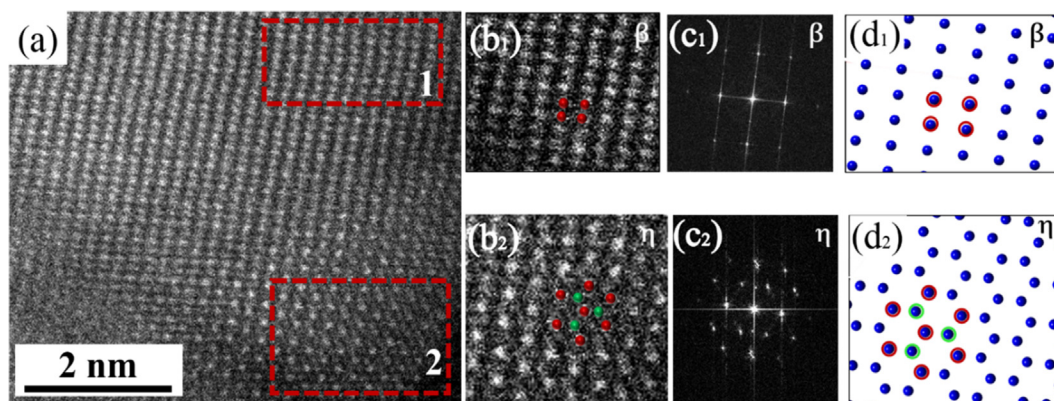
Fig. 6 (a) shows the STEM-HAADF micrograph of the ECP induced  $\beta$  precipitate acquired with the incident-beam parallel to the  $[011]_{\beta}$ . The atomic arrangement zones corresponding to the BCC  $\beta$  structure (Zone 1) and the  $\eta$  structure (Zone 2) are well visible, as outlined with the red dashed rectangles in Fig. 6 (a) and further magnified in Fig. 6 (b) (labeled with the same numbers as in Fig. 6 (a)). The corresponding Fast Fourier transform (FFT) image serving as the diffraction patterns of these zones and the  $[011]_{\beta}$  projection of the atom columns of the two structures are given in Fig. 6 (c) and (d) (labeled with the same numbers as in Fig. 6 (a)). Comparing the FFT images in Fig. 6 (c<sub>2</sub>) with the diffraction pattern of the  $\eta$  structure in Fig. 5 (a) and the atomic arrangement in Fig. 6 (b<sub>2</sub>) with that in Fig. 6 (d<sub>2</sub>), the  $\eta$  structure in Zone 2 is confirmed.

Fig. 7 (a) shows a STEM-HAADF micrograph of the ECP induced  $\beta$  precipitate acquired with the  $[011]_{\beta}$  parallel to the incident-beam. Two characteristic atomic arrangements possessing the BCC  $\beta$  structure and the  $\omega$  structure are outlined with the respective red rectangles (Zone 1 and 2) and further magnified in Fig. 7 (b) with the corresponding FFT image in Fig. 7 (c) (labeled with the same numbers as in Fig. 7 (a)). Zone 1 demonstrates the perfect  $\beta$  atomic arrangement in the BCC structure. The FFT image in Fig. 7 (c<sub>1</sub>) well reproduces the  $[011]_{\beta}$  zone axis SAED pattern. For reference, the projected atom columns from the perfect  $\beta$  structure is shown in Fig. 7 (d<sub>1</sub>). It is seen that the projection of the atom columns (Fig. 7 (d<sub>1</sub>)) well corresponds to the images of the  $\beta$  phase in Zone 1 (Fig. 7 (b<sub>1</sub>)). Zone 2 corresponds to the  $\omega$  structure. The FFT image in Fig. 7 (c<sub>2</sub>) well reproduces the SAED pattern of the  $\omega$  structure in the  $[011]_{\beta}$  zone axis SAED pattern, i.e., the appearance of the additional spots at the  $1/3$  and  $2/3$   $\{112\}_{\beta}$  reflection positions. For reference, the projected atom columns from the perfect  $\beta$ ,  $\eta$  and  $\omega$  structures are shown in Fig. 7 (d<sub>1</sub>), (d<sub>2</sub>) and (d<sub>4</sub>). Further analysis showed that Zone 2 corresponds to the  $\eta$  structure, whereas Zone 4 to the  $\omega$  structure. It should be noted that when the incident beam is in the  $[010]_{\beta}$  direction of the  $\beta$  phase, the corresponding direction of the  $\omega$  structure is the  $[0.110\bar{3} \ 0.1103 \ 0 \ 0.2229]_{\omega}$ . This zone axis diffraction pattern of  $\omega$  is superimposed with the  $[010]_{\beta}$  zone axis diffraction pattern of  $\beta$ . Thus in the  $[010]_{\beta}$  zone axis SAED pattern in Fig. 4 (a), we could not differentiate the diffraction spots of the  $\omega$  structure from those of the  $\beta$  phase. However, in the STEM-HAADF micrograph in Fig. 8 (a), we can easily find the existence of the  $\omega$  struc-

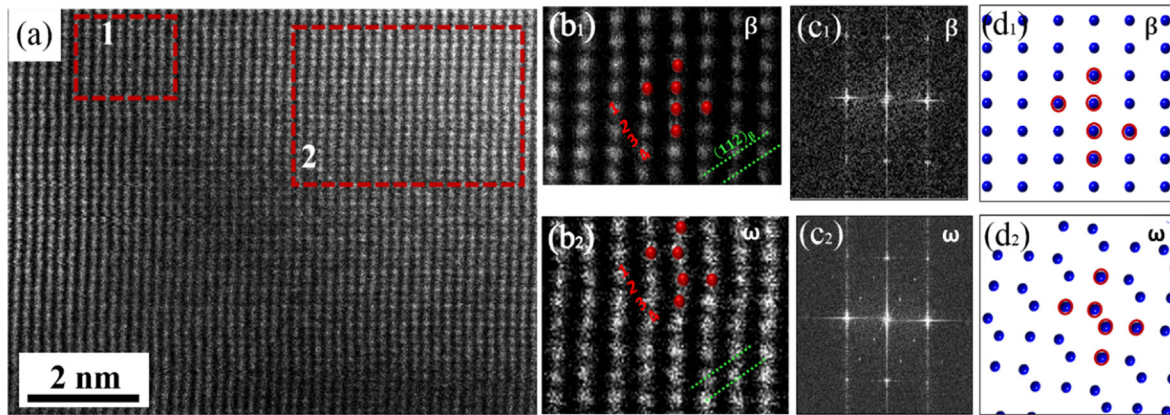
ture that the structure giving the  $\omega$  diffraction is in the course of the transition from the BCC  $\beta$  structure to the hexagonal  $\omega$  structure.

Furthermore, the lattice constants of the  $\beta$ ,  $\eta$  and  $\omega$  structures were measured from the STEM-HAADF micrographs and listed in Table 2. These measured lattice constants of the three structures allow accurate analyses of the lattice strains for the structure transformation, as will be demonstrated later. It should be noted that the standard deviations displayed in the table indicate rather the lattice constant deviations than measurement errors. The relatively large spread of the lattice constants demonstrates the existence of structure fluctuations in the two hexagonal distortions. During the lattice constant measurement, we found that the fluctuation zones are very local involving only 2 or 3 atoms in each measured atom row. In the long range the negative and positive fluctuations tend to cancel out each other and the lattice constants converge to the average values.

To further analyze the transition of the atomic shuffles or displacements from the  $\beta$  structure to the two hexagonal structures and their spatial relation, the atomic arrangements of the two hexagonal structures in the  $[001]_{\beta}$  zone axis STEM-HAADF micrographs were examined. Fig. 8 (a) shows an example of the STEM-HAADF micrograph of the ECP induced  $\beta$  precipitate acquired with the  $[001]_{\beta}$  parallel to the incident-beam where the two structures co-exist in the  $\beta$  matrix. In the figure, the characteristic atomic arrangement zones of the BCC  $\beta$  structure (Zone 1), the  $\eta$  structure (Zone 2) and the near  $\omega$  structure (Zone 4), and the zones presenting the lattice deformation in the course to change from the BCC  $\beta$  to the respective two structures (Zone 3 and 5) are well present, as outlined with the red dashed rectangles in Fig. 8 (a) and further magnified in Fig. 8 (b) (labeled with the same numbers as in Fig. 8 (a)). The corresponding FFT images serving as the diffraction patterns of these zones are given in Fig. 8 (c) (labeled with the same numbers as in Fig. 8 (a)). For reference, the projected atom columns from the perfect  $\beta$ ,  $\eta$  and  $\omega$  structures are shown in Fig. 8 (d<sub>1</sub>), (d<sub>2</sub>) and (d<sub>4</sub>). Further analysis showed that Zone 2 corresponds to the  $\eta$  structure, whereas Zone 4 to the  $\omega$  structure. It should be noted that when the incident beam is in the  $[010]_{\beta}$  direction of the  $\beta$  phase, the corresponding direction of the  $\omega$  structure is the  $[0.110\bar{3} \ 0.1103 \ 0 \ 0.2229]_{\omega}$ . This zone axis diffraction pattern of  $\omega$  is superimposed with the  $[010]_{\beta}$  zone axis diffraction pattern of  $\beta$ . Thus in the  $[010]_{\beta}$  zone axis SAED pattern in Fig. 4 (a), we could not differentiate the diffraction spots of the  $\omega$  structure from those of the  $\beta$  phase. However, in the STEM-HAADF micrograph in Fig. 8 (a), we can easily find the existence of the  $\omega$  struc-



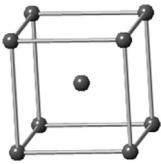
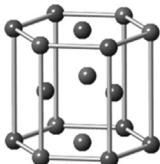
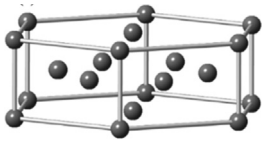
**Fig. 6.** (a) STEM-HAADF micrograph of the ECP induced  $\beta$  precipitates viewed in the  $[011]_{\beta}$  direction. (b<sub>1</sub>) and (b<sub>2</sub>) A typical example of the regions marked with rectangles 1 and 2, respectively. (c<sub>1</sub>) and (c<sub>2</sub>) The Fast Fourier Transform of the regions marked by rectangles 1 and 2, respectively. (d<sub>1</sub>) and (d<sub>2</sub>) The simulated projection of the atom columns from the corresponding ideal structures of BCC  $\beta$  and hexagonal  $\eta$ , respectively. For the  $\eta$  structure, the red symbols mark the atomic positions on the upper layer, whereas the green ones outline the atomic positions in the lower layer. (For interpretation of the references to colour in this figure legend, the reader is referred to the web version of this article.)



**Fig. 7.** (a) STEM-HAADF micrograph of the  $\beta$  matrix viewed in the  $[011]_{\beta}$  direction in the ECP induced  $\beta$  precipitates of the Cu-40 %Zn alloy. (b<sub>1</sub>) and (b<sub>2</sub>) A typical example of the regions marked by rectangles 1 and 2, respectively. (c<sub>1</sub>) and (c<sub>2</sub>) The Fast Fourier Transform from the regions marked with rectangles 1 and 2, respectively. (d<sub>1</sub>) and (d<sub>2</sub>) The projection of the simulated atom columns from the corresponding perfect  $\beta$  and  $\omega$  structures. The atomic cells are marked with the red symbols. (For interpretation of the references to colour in this figure legend, the reader is referred to the web version of this article.)

**Table 2**

Lattice constants of  $\beta$ ,  $\eta$  and  $\omega$  structures in ECPed Cu-40 %Zn sample and the illustration of the crystal structures. The data were counted from 20 atom rows from each of 6 images that were taken with the incident beam either parallel to the  $[011]_{\beta}$  or to the  $[001]_{\beta}$  direction. For  $\beta$  phase, the  $(110)_{\beta}$ ,  $(200)_{\beta}$ ,  $(130)_{\beta}$  and  $(112)_{\beta}$  planes were used to measure the lattice parameter  $a_{\beta}$ . For the  $\eta$  structure, the  $(0002)_{\eta}$ ,  $(0111)_{\eta}$ ,  $(1010)_{\eta}$  and  $(1100)_{\eta}$  planes were used, and, for the  $\omega$  structure, the  $(0001)_{\omega}$ ,  $(0010)_{\omega}$  and  $(0111)_{\omega}$  planes were used. The standard deviations indicate rather the spread of the lattice constants than the measurement errors.

	$\beta$	$\eta$	$\omega$
a	$2.91 \pm 0.06 \text{ \AA}$	$2.53 \pm 0.05 \text{ \AA}$	$4.09 \pm 0.11 \text{ \AA}$
c	/	$4.47 \pm 0.31 \text{ \AA}$	$2.51 \pm 0.07 \text{ \AA}$
Average c/a	/	1.75	0.61
Structure			

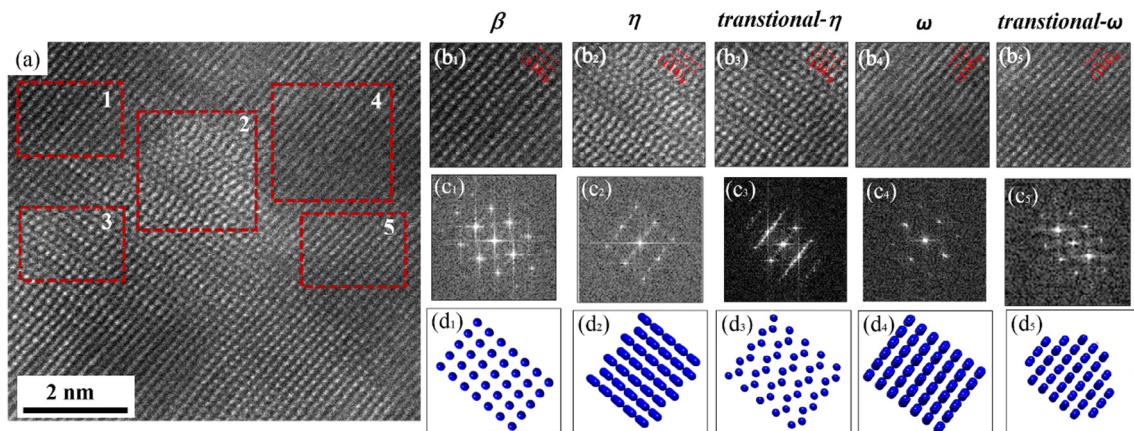


**Fig. 8.** (a) STEM-HAADF micrographs of the matrix viewed in the  $[001]_{\beta}$  direction in the ECP induced  $\beta$  precipitates of the Cu-40 %Zn alloy after the ECP treatment. (b<sub>1</sub>), (b<sub>2</sub>), (b<sub>3</sub>), (b<sub>4</sub>) and (b<sub>5</sub>) A typical example of the regions marked by rectangles 1, 2, 3, 4 and 5, respectively. (c<sub>1</sub>), (c<sub>2</sub>), (c<sub>3</sub>), (c<sub>4</sub>) and (c<sub>5</sub>) Fast Fourier Transforms performed in the regions marked by the rectangles 1, 2, 3, 4 and 5, respectively. (d<sub>1</sub>), (d<sub>2</sub>), (d<sub>3</sub>), (d<sub>4</sub>) and (d<sub>5</sub>) The simulated atom column projections from the corresponding perfect structures, respectively.

ture. Moreover, we can find that the two structures ( $\eta$  and  $\omega$ ) have neither fixed borders nor constant shape but they are always located next to each other, suggesting that they are concomitant. In either of the zones, the two hexagonal structures are also not constant. With the spread-out of the two structures, the atom positions change from the more or less perfect hexagonal structures to

the perfect BCC structure of the  $\beta$  phase. Thus, the transition regions between the  $\beta$  structure and either of the two structures can be regarded as structure transition regions that can also be considered as specifically deformed  $\beta$  structure. For example, Zone 3 in Fig. 8 (a) can be regarded as the transition structure toward the  $\eta$  structure, as it is in the continuity of the corresponding



structure. Zone 5 in Fig. 8 (a) can be regarded as the transition structure toward the  $\omega$  structure, as it is in the continuity of the corresponding structure. As the transitional zones are specifically deformed  $\beta$  structure, characteristic streaks will appear at the  $\beta$  diffraction spots in the SAED patterns that can be used to analyze the lattice deformation features, as detailed in the next section.

### 3.3. Identification of atomic shuffling and displacement system to realize the structure change

As the formation of the two structures is realized by atomic displacement or shuffle, it is important to identify the displacement or shuffle systems (plane and direction) to understand the formation of the transitional structures and the final structure change. The transitional regions that can be regarded as the deformed  $\beta$  structure would modify the shape of the diffraction spots of the  $\beta$  phase, and thus the shape characters of the  $\beta$  diffraction spots allow obtaining the required information. Fig. 9 and Fig. 10 display several characteristic  $\beta$  zone axis TEM SAED patterns ( $[010]_{\beta}$ – $[011]_{\beta}$  in Fig. 9 and  $[111]_{\beta}$ – $[113]_{\beta}$  in Fig. 10). It is seen that apart from the fine streaks passing through all the diffraction spots including the origin (the transmitted beam) there are another two features associated with the diffraction spots of the  $\beta$  phase. The first is that the  $\beta$  diffraction spots are all elongated in certain reciprocal directions, forming the so-called relrods and the elongation increases with the increasing order of diffraction, as indicated by the yellow arrow in Fig. 10 (a), as an example. The second is that the relrods exhibit characteristic extinction [39]. These features suggest that the appearance of the relrods is from planar crystal defects [40] that should be related to the atomic shuffle or displacement. Systematic examination revealed that the  $\beta$  spots are elongated in two families of reciprocal directions  $\langle 110 \rangle_{\beta}$  and  $\langle 112 \rangle_{\beta}$ , as indicated with the respective red and green bars in Figs. 9 and 10. It has well been established that the atomic displacement or shuffle in certain directions on the atomic planes will result in the extension of the diffracted intensity along the normal to the shear planes. The two reciprocal directions in the present work correspond to the normal of two crystalline planes of the  $\beta$  phase, i.e., the  $\{110\}_{\beta}$  and  $\{112\}_{\beta}$  plane, as the  $\beta$  phase possesses a cubic structure. This evidences that there exists atomic displacement or shuffle on the  $\{110\}_{\beta}$  and  $\{112\}_{\beta}$  phase.

It is also well established in the theory of electron diffraction that if the vector of the atomic displacement (resembling dislocation Burgers vector) on the plane (denoted  $\mathbf{u}$  in the present work) is lying on the planes of the operating reflections, the extended diffraction intensity (corresponding to the relrod) from the faulted

plane will disappear, i.e., the relrod that is parallel to the normal of the shear plane disappear from the diffraction spots. So the characteristic extinction of the relrods allow finding the displacement vectors or the displacement directions. In the two zone axis patterns in Fig. 9 the  $\langle 110 \rangle_{\beta}$  relrods exist in the  $[010]_{\beta}$  pattern but not in the  $[011]_{\beta}$  pattern although in the two patterns the  $\langle 110 \rangle_{\beta}$  reciprocal direction exist (the  $\pm [01\bar{1}]_{\beta}$  reciprocal direction in Fig. 9 (b)), evidencing the extinction of the  $[01\bar{1}]_{\beta}$  relrod. However, in the two zone axis patterns in Fig. 10, the  $\langle 112 \rangle_{\beta}$  relrods are present in the  $[011]_{\beta}$  pattern but not in the  $[010]_{\beta}$  pattern although the  $\langle 112 \rangle_{\beta}$  reciprocal directions present in the two patterns. This evidences the extinction of the  $\langle 112 \rangle_{\beta}$  relrods. To find out the possible displacement vectors on the two faulted planes, we verified the invisibility of all the dislocation Burgers vectors published in the literature ( $\langle 112 \rangle$ ,  $\langle 101 \rangle$ ,  $\langle 111 \rangle$ ) in the BCC crystals for the reflections in the two zone axes (the  $[011]_{\beta}$  zone axis reflections for the  $\{110\}_{\beta}$  extinctions and the  $[111]_{\beta}$  zone axis reflections for the  $\{112\}_{\beta}$  extinctions). The results show that the extinction of the  $\langle 110 \rangle_{\beta}$  relrods at the reflections in the  $[011]_{\beta}$  zone axis (Fig. 9 (b)) is from the  $\langle 011 \rangle_{\beta}$  displacement on the  $\{110\}_{\beta}$ , as shown in Table 3. The  $\mathbf{u} \cdot \mathbf{g} = 0$  is fulfilled for all the reflections in the  $[011]_{\beta}$  axis zone (highlighted in bold) but is not for those in the  $[010]_{\beta}$  zone axis. This indicates that the formation of the  $\langle 110 \rangle_{\beta}$  relrods is originated from the atomic shuffle or displacement on the  $(01\bar{1})_{\beta}$  plane in the  $[011]_{\beta}$  direction. This result evidences the activation of the  $\{110\}_{\beta} < 1\bar{1}0 \rangle_{\beta}$  shuffle or shear system in the  $\beta$  precipitates. However, the extinction of the  $\langle 112 \rangle_{\beta}$  relrods at the reflections in the  $[111]_{\beta}$  zone axis (Fig. 10 (a)) is from the atomic displacement in the  $[111]_{\beta}$  direction, as shown in Table 4. The  $\mathbf{u} \cdot \mathbf{g} = 0$  is fulfilled for all the reflections in the  $[111]_{\beta}$  zone axis (highlighted in bold) but not for those in the  $[113]_{\beta}$  zone axis. This indicates that the formation the  $\langle 112 \rangle_{\beta}$  relrods is originated from the atomic shuffle or displacement on the  $(11\bar{2})_{\beta}$  plane in the  $[111]_{\beta}$  direction. This result evidences the activation of the  $\{112\}_{\beta} < 1\bar{1}1 \rangle_{\beta}$  shuffle or shear system in the  $\beta$  precipitates. The atomic shuffles or displacement on these two systems should be related to the low energy or soft phonon modes in the BCC structure, as have been revealed by many experimental and theoretical investigations [2,7,21,29]. Thus, the two kinds of atomic shuffle or displacement in the present work should be in relation with the formation of the  $\eta$  and  $\omega$  structures in the  $\beta$  precipitates.

Based on the revealed shuffle systems and the orientation relationships between the parent  $\beta$  precipitates and the two structures, i.e., the Burgers OR between the  $\beta$  structure and the hexagonal  $\eta$  structure and the Blackburn OR between the  $\beta$  and the  $\omega$  structure,

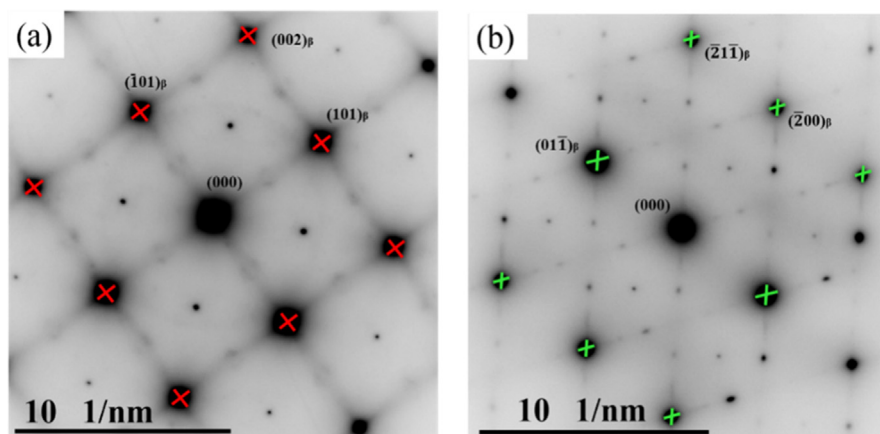
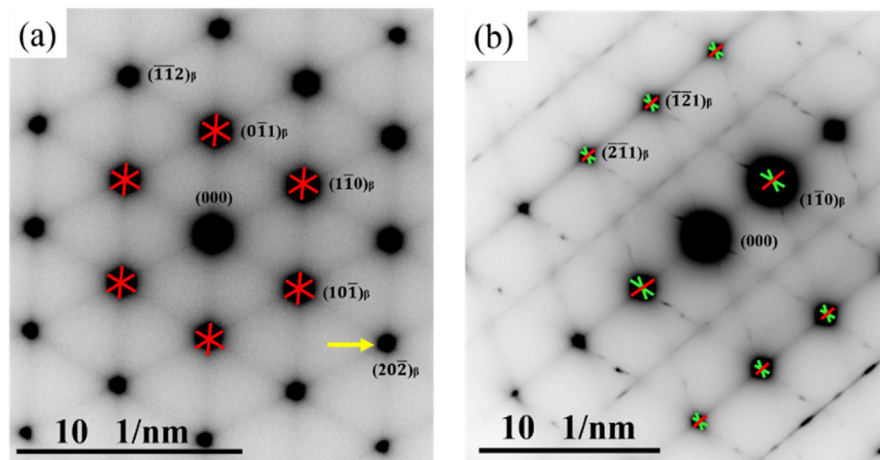


Fig. 9. TEM SAED patterns of (a) the  $[010]_{\beta}$  and (b) the  $[011]_{\beta}$  zone axis of the ECP induced  $\beta$  precipitates. The  $\langle 110 \rangle_{\beta}$  relrods are marked in red and the  $\langle 112 \rangle_{\beta}$  relrods are marked in green. (For interpretation of the references to colour in this figure legend, the reader is referred to the web version of this article.)



**Fig. 10.** TEM SAED patterns of (a) the  $[111]_{\beta}$  and (b) the  $[113]_{\beta}$  zone axis of the ECP induced  $\beta$  precipitates. The  $\langle 110 \rangle_{\beta}$  relrods are marked in red and the  $\langle 112 \rangle_{\beta}$  relrods are marked in green. The yellow arrow in (a) indicates an example of the increased streaking of the  $(202)_{\beta}$  spot. (For interpretation of the references to colour in this figure legend, the reader is referred to the web version of this article.)

**Table 3**  
 $\mathbf{g} \cdot \mathbf{u}$  for the reflections in  $[010]_{\beta}$  and  $[011]_{\beta}$  zone axis diffraction patterns of ECP induced  $\beta$  phase.

Shear plane	Zone axis		$[010]_{\beta}$			$[011]_{\beta}$		
	$\mathbf{u}$	$\mathbf{g}$	$(101)_{\beta}$	$(002)_{\beta}$	$(\bar{1}01)_{\beta}$	$(\bar{2}1\bar{1})_{\beta}$	$(\bar{2}00)_{\beta}$	$(01\bar{1})_{\beta}$
$(01\bar{1})_{\beta}$	$[011]_{\beta}$		$\neq 0$	$\neq 0$	$\neq 0$	<b>=0</b>	<b>=0</b>	<b>=0</b>
$(1\bar{1}0)_{\beta}$	$[110]_{\beta}$		$\neq 0$	$=0$	$\neq 0$	$\neq 0$	$\neq 0$	$\neq 0$
$(110)_{\beta}$	$[\bar{1}10]_{\beta}$		$\neq 0$	$=0$	$\neq 0$	$\neq 0$	$\neq 0$	$\neq 0$
$(011)_{\beta}$	$[0\bar{1}1]_{\beta}$		$\neq 0$	$=0$	$\neq 0$	$\neq 0$	$=0$	$\neq 0$
$(10\bar{1})_{\beta}$	$[101]_{\beta}$		$\neq 0$	$\neq 0$	$=0$	$\neq 0$	$\neq 0$	$\neq 0$
$(101)_{\beta}$	$[\bar{1}01]_{\beta}$		$=0$	$\neq 0$	$\neq 0$	$\neq 0$	$\neq 0$	$\neq 0$

**Table 4**  
 $\mathbf{u}$  for reflections in  $[111]_{\beta}$  and  $[113]_{\beta}$  zone axis diffraction patterns of ECP induced  $\beta$  phase.

Shear plane	Zone axis		$[111]_{\beta}$				$[113]_{\beta}$		
	$\mathbf{u}$	$\mathbf{g}$	$(10\bar{1})_{\beta}$	$(1\bar{1}0)_{\beta}$	$(0\bar{1}1)_{\beta}$	$(\bar{1}\bar{1}2)_{\beta}$	$(1\bar{1}0)_{\beta}$	$(\bar{2}\bar{1}1)_{\beta}$	$(\bar{1}\bar{2}1)_{\beta}$
$(11\bar{2})_{\beta}$	$[111]_{\beta}$		<b>=0</b>	<b>=0</b>	<b>=0</b>	<b>=0</b>	$=0$	$\neq 0$	$\neq 0$
$(\bar{2}11)_{\beta}$	$[\bar{1}11]_{\beta}$		$\neq 0$	$\neq 0$	$=0$	$\neq 0$	$\neq 0$	$\neq 0$	$=0$
$(121)_{\beta}$	$[1\bar{1}1]_{\beta}$		$=0$	$\neq 0$	$\neq 0$	$\neq 0$	$\neq 0$	$=0$	$\neq 0$
$(112)_{\beta}$	$[\bar{1}\bar{1}1]_{\beta}$		$\neq 0$	$=0$	$\neq 0$	$\neq 0$	$=0$	$\neq 0$	$\neq 0$

the atomic correspondences of the transition structures or the deformed  $\beta$  structure to form the two hexagonal structures ( $\eta$  and  $\omega$ ) were further established, as shown in Fig. 11 and Fig. 12, where the two end structures (the perfect  $\beta$  structure and the perfect hexagonal structure are also displayed as references). Careful examination of the lattice distortion, we can find that each structure change involves a two-step atomic displacement.

For the  $\beta$  to  $\eta$  structure change, the first step is the atomic displacement of each second basal layer, the  $\{110\}_{\beta}$  (circled in yellow in Fig. 11 (a) and (b)), in the  $\langle 1\bar{1}0 \rangle_{\beta}$  direction by an amount of  $a/4 \langle 1\bar{1}0 \rangle_{\beta}$ . Thus, we obtain an intermediate structure that is orthorhombic, as shown in Fig. 11 (b). The second step is the atomic displacement of the two neighboring  $\{110\}_{\beta}$  planes (parallel to the yellow circled planes in Fig. 11 (a)) to the hexagonal structure (Fig. 11 (c)). Then we project the intermediate  $\eta$  structure along the  $\langle 001 \rangle_{\beta}$  direction and display it in Fig. 8 (d<sub>3</sub>). Comparing the projected atom columns in Fig. 8 (d<sub>3</sub>) with the STEM-HAADF images in Fig. 8 (b<sub>3</sub>), one can see the good coincidences

between the two. This confirms that the formation of the transitional structure of  $\eta$  is indeed realized by the atomic displacement on every second  $\{110\}_{\beta}$  and in the  $\langle 1\bar{1}0 \rangle_{\beta}$  direction and validates the two-step structure change.

The similar analysis was also conducted for the  $\beta$  to  $\omega$  structure change. This structure change also progresses in two steps. The first step is the atomic shuffle of each second and third  $\{112\}_{\beta}$  planes (circled in green for the second layer and circled in black for the third layer in Fig. 12 (a) and (b)), in the  $\pm [111]_{\beta}$  direction by an amount of  $a/12[111]_{\beta}$ . The second step is the further atomic distortions of the two neighboring  $\{112\}_{\beta}$  planes (the prismatic planes marked with green dotted lines in Fig. 12 (a)) to the hexagonal structure (Fig. 12 (c)). Then, we project the intermediate  $\omega$  structure along the  $\langle 001 \rangle_{\beta}$  direction and display it in Fig. 8 (d<sub>5</sub>). Comparing the projected atom columns in Fig. 8 (d<sub>5</sub>) with the STEM-HAADF image in Fig. 8 (b<sub>5</sub>), one can see the good coincidences between the atomic arrangement in the STEM-HAADF image and the simulated projection. This further validates the two-stepped structure change.



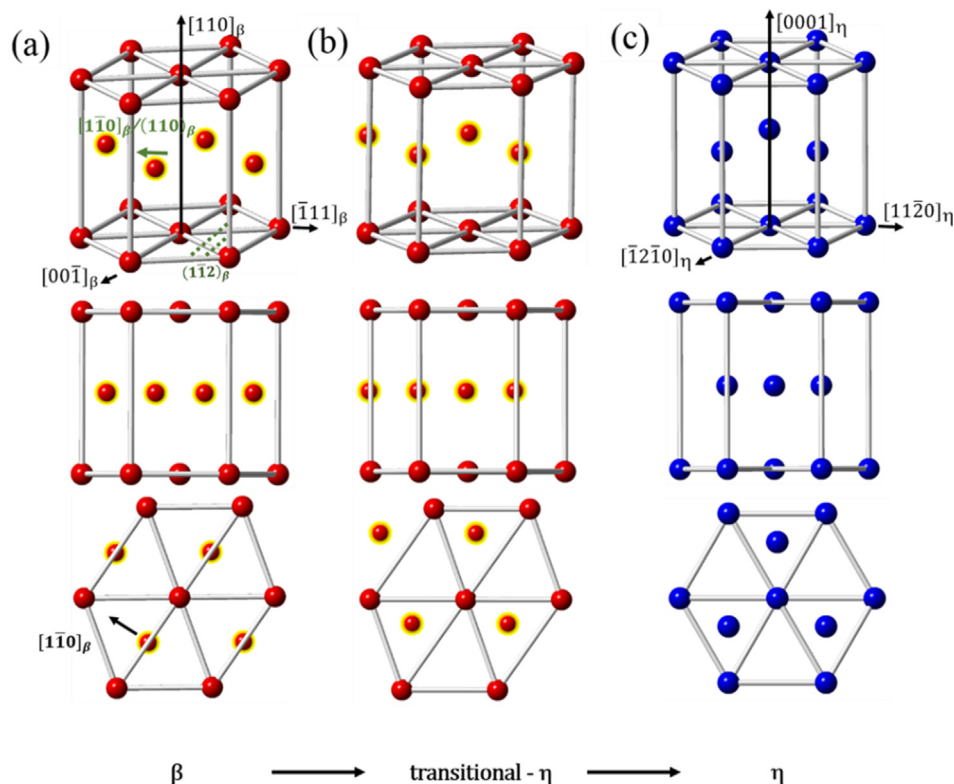


**Fig. 11.** 3D, front view and top view of the atomic correspondences between the  $\beta$  (a) and the  $\eta$  (c) structure under the Burgers OR. The atoms of the parent  $\beta$  structure are in red and those of the product  $\eta$  structure in blue. The displaced atoms for the structure change in the first step are marked with yellow circles. (For interpretation of the references to colour in this figure legend, the reader is referred to the web version of this article.)

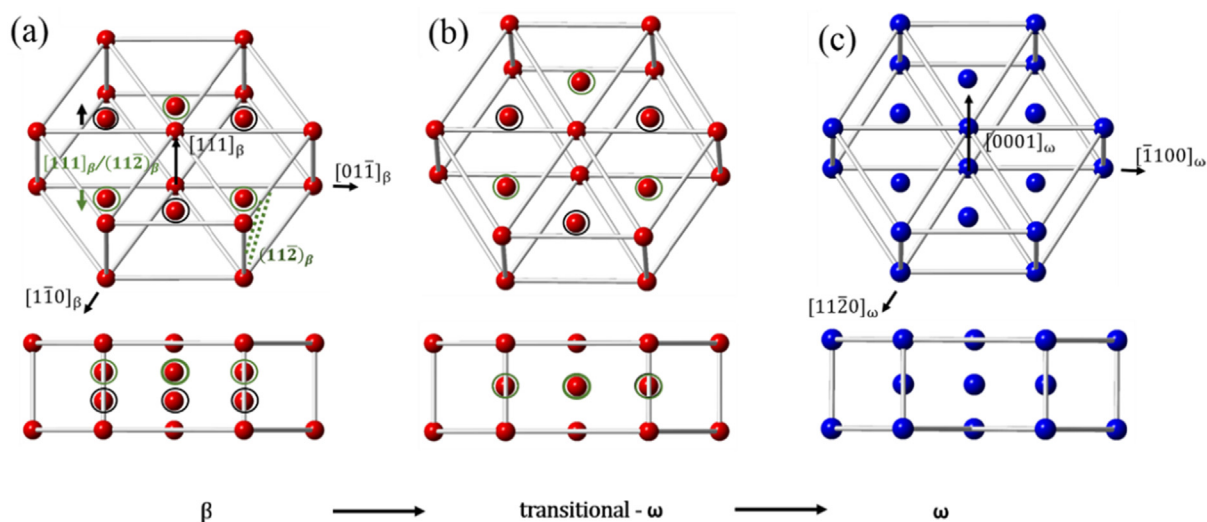


**Fig. 12.** 3D and front view of the atomic correspondences between the  $\beta$  (a) and the  $\omega$  structure (c) under the Blackburn OR. The atoms of the parent  $\beta$  structure are in red and those of the product  $\omega$  structure in blue. The displaced atoms in the first step of the structure change are marked with green (for the second  $\{11\bar{2}\}$  layer) and black (for the third  $\{11\bar{2}\}$  layer) circles. The first  $\{11\bar{2}\}$  plane is shaded with the green dotted lines. (For interpretation of the references to colour in this figure legend, the reader is referred to the web version of this article.)  $\beta$

### 3.4. Origin of concomitant formation of the two hexagonal structures

As the formation of the two structures is realized by atomic shuffle or displacement, the co-existence of the two structures should be related to the lattice deformation associated to the structure transformation. Thus, the lattice strains to form the  $\eta$  structure and the  $\omega$  structure under the respective ORs were ana-

lyzed using the lattice constants list in Table 2 and represented with the deformation gradient tensor expressed in the corresponding OR reference system ( $i-j-k$ ) (as illustrated in Fig. 13) and displayed in Table 5. It should be mentioned that the lattice deformation described by the tensors for the two structures is only applicable to the second step of the structure change. This further confirms that the formation of the two new structures progresses

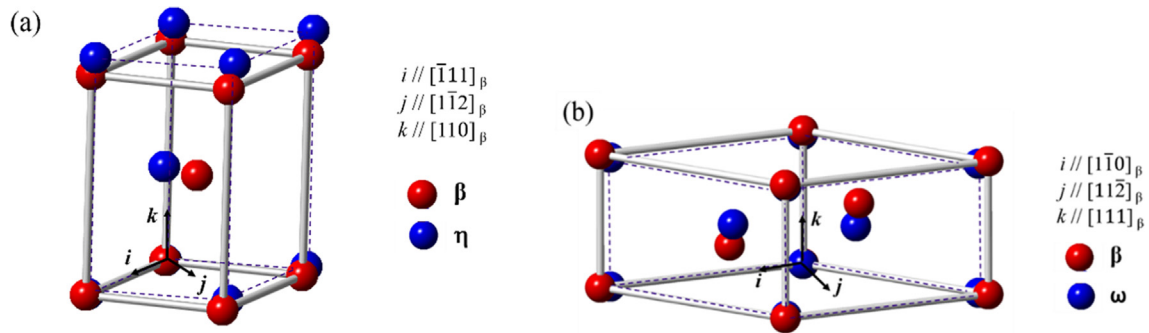


**Fig. 13.** Atomic correspondences (a) between the  $\beta$  and the  $\eta$  structure under the Burgers OR and (b) between the  $\beta$  and the  $\omega$  structure under the Blackburn OR. The OR reference systems ( $i$ - $j$ - $k$ ) are set with direction  $i$  parallel to the OR direction,  $k$  to the direction normal to the OR plane and  $j$  to the vector cross product of  $k$  and  $i$ . The atoms of the parent  $\beta$  phase are in red and those of the product structures ( $\eta$ ;  $\omega$ ) in blue. (For interpretation of the references to colour in this figure legend, the reader is referred to the web version of this article.)

**Table 5**

Deformation gradient tensors of structure deformation in the second-step to form the two structures expressed in the corresponding OR reference frame taking account of the lattice constant spread. AVG stands for average lattice constants, MAX upper limit of the lattice constants and MIN lower limit of the lattice constants.

$\beta \rightarrow \eta$			
$\{110\}_{\beta} // \{0001\}_{\eta} < \bar{1}11 >_{\beta} // < 11 \bar{2} 0 >_{\eta}$			
Lattice constants	Deformation Gradient Tensor	Volume change	
	$i // [\bar{1}11]_{\beta} \quad j // [1\bar{1}2]_{\beta} \quad k // [110]_{\beta}$		
MAX	$a_{\beta} = 2.97$ $a_{\eta} = 2.58$ $c_{\eta} = 4.78$	$\begin{bmatrix} 1.0031 & -0.1773 & 0 \\ 0 & 0.9214 & 0 \\ 0 & 0 & 1.1380 \end{bmatrix}$	5.18%
AVG	$a_{\beta} = 2.91$ $a_{\eta} = 2.53$ $c_{\eta} = 4.47$	$\begin{bmatrix} 1.0039 & -0.1775 & 0 \\ 0 & 0.9222 & 0 \\ 0 & 0 & 1.0862 \end{bmatrix}$	0.55%
MIN	$a_{\beta} = 2.85$ $a_{\eta} = 2.48$ $c_{\eta} = 4.17$	$\begin{bmatrix} 1.0048 & -0.1776 & 0 \\ 0 & 0.9230 & 0 \\ 0 & 0 & 1.0346 \end{bmatrix}$	-4.05%
$\beta \rightarrow \omega$			
$\{111\}_{\beta} // \{0001\}_{\omega} < 1 \bar{1} 0 >_{\beta} // < 11 \bar{2} 0 >_{\omega}$			
Lattice constants	Deformation Gradient Tensor	Volume change	
	$i // [1\bar{1}0]_{\beta} \quad j // [11\bar{2}]_{\beta} \quad k // [111]_{\beta}$		
MAX	$a_{\beta} = 2.97$ $a_{\eta} = 4.10$ $c_{\eta} = 2.58$	$\begin{bmatrix} 0.9766 & 0 & 0 \\ 0 & 0.9766 & 0 \\ 0 & 0 & 1.0031 \end{bmatrix}$	-4.33%
AVG	$a_{\beta} = 2.91$ $a_{\eta} = 4.09$ $c_{\eta} = 2.51$	$\begin{bmatrix} 0.9941 & 0 & 0 \\ 0 & 0.9941 & 0 \\ 0 & 0 & 0.9960 \end{bmatrix}$	-0.15%
MIN	$a_{\beta} = 2.85$ $a_{\eta} = 4.08$ $c_{\eta} = 2.44$	$\begin{bmatrix} 1.0123 & 0 & 0 \\ 0 & 1.0123 & 0 \\ 0 & 0 & 0.9886 \end{bmatrix}$	1.30%

in two steps. The first step is realized by the atomic shuffle on the two shear systems other than the deformation described by the tensors in Table 5.

It is seen from Table 5 that for the formation of the  $\eta$  structure it requires an respective elongations in the  $[\bar{1}11]_{\beta}$  direction ( $0.39\%^{+0.09\%}_{-0.08\%}$ ) and in the  $[110]_{\beta}$  direction ( $8.62\%^{+5.18\%}_{-5.16\%}$ ) and a contraction in the  $[1\bar{1}2]_{\beta}$  direction ( $7.78\% \pm 0.08\%$ ). The transformation also requires a shear of  $-0.1175^{+0.0002}_{-0.0001}$  on the  $(1\bar{1}2)_{\beta}$  plane and in the  $[\bar{1}11]_{\beta}$  direction. Thus the soft  $\{110\}_{\beta} < 1 \bar{1} 0 >_{\beta}$  system allows the atomic shuffle to form the transition structure of the  $\eta$  structure (Fig. 11 (b)) and the soft shear system  $\{1\bar{1}2\}_{\beta} < \bar{1}11 >_{\beta}$  allows finalizing the structure transformation. However, the formation of the  $\eta$  structure yields a volume increase by  $0.55\%^{+4.63\%}_{-4.60\%}$  on average that is unfavorable during the cooling process, as by thermal dilatation, the overall volume of the material diminishes.

For the  $\omega$  structure, the transformation requires the  $\beta$  lattice to contract in the three principle directions: the  $[1\bar{1}0]_{\beta}$  direction (by  $0.59\%^{+1.82\%}_{-1.75\%}$ ), the  $[11\bar{2}]_{\beta}$  direction (by  $0.59\%^{+1.82\%}_{-1.75\%}$ ) and the  $[111]_{\beta}$  direction (by  $0.40\%^{+0.71\%}_{-0.74\%}$ ), as summarized in Table 5. No shear is required. However, the formation of the  $\omega$  structure yields a volume shrinkage (by  $0.15\%^{+1.45\%}_{-4.18\%}$ ). This volume shrinkage should effectively cancel the volume increase of the formation of the  $\eta$  structure that is unfavorable during the cooling process. It should be noted that the volumic fluctuations induced by lattice constant spread given in Table 5 seems to be very pronounced but in reality, such fluctuation happened very locally involving only several atoms. Clearly, the soft shear system  $\{11\bar{2}\}_{\beta} < 111 >_{\beta}$  allows the atomic shuffle on this system to achieve the first step of the  $\omega$  structure change. Thus, the  $\omega$  structure should be formed accompanying the formation of the  $\eta$  structure to minimize the lattice distortion of each single formation. As any lattice distortion results in an increase of the elastic energy, the minimization of the lattice distortion through the concomitant formation of the two structures surely decreases the overall elastic energy of the two structures and thus favors their co-existence.

#### 4. Summary

In the present work, the formation mechanisms of the two nano-sized hexagonal structures ( $\eta$  and  $\omega$ ) in the ECP induced  $\beta$  precipitates in a Cu-40Zn alloy was thoroughly investigated. The results demonstrate that the two kinds of hexagonal structures were formed by lattice deformation. The two structures are commonly featured with atomic clusters without fixed shape nor clear boundary with the  $\beta$  matrix and connected with the  $\beta$  matrix by structural transition regions.

For the  $\eta$  structure, it possesses a crystal structure of the Cu<sub>2</sub>Zn<sub>98</sub> phase and obeys the Burgers OR with the  $\beta$  matrix. The formation of this structure involves two steps of lattice deformation. The first is the atomic shuffle on each second  $\{110\}_{\beta}$  plane in the  $< \bar{1}10 >_{\beta}$  direction. Such atomic shuffle transforms the BCC structure of the  $\beta$  phase to an orthorhombic structure that exists in the transition regions between the matrix  $\beta$  and the  $\eta$  structure and produces the  $< \bar{1}10 >_{\beta}$  reldrods in the TEM SAED patterns. The second step is to realize the structure change from the transitional orthorhombic structure to the hexagonal structure by mainly a shear on the  $\{1\bar{1}2\}_{\beta}$  plane in the  $< \bar{1}11 >_{\beta}$  direction accompanied by small normal strains in the shear plane normal direction ( $(112)_{\beta}$ ), in the shear direction ( $< 1 \bar{1} 1 >_{\beta}$ ) and in the direction normal to these two ( $< 110 >_{\beta}$ ).

For the  $\omega$  structure, it possesses the crystal structure of the CuZn<sub>3</sub> phase and obeys the Blackburn OR with the  $\beta$  matrix. The

formation of this structure involves also two steps of lattice deformation. The first is the atomic shuffle on each second and third  $\{11\bar{2}\}_{\beta}$  planes in the  $\pm [111]_{\beta}$  direction, which creates an hexagonal structure. Such a structure constitutes of the transition regions between the matrix  $\beta$  and the  $\omega$  structure and produces the  $(112)_{\beta}$  relrods in the TEM SAED patterns. The second step is to realize the structure change from the transitional hexagonal structure to the final hexagonal structure by three normal strains in the shuffle plane normal direction ( $111_{\beta}$ ), in the shuffle direction ( $11\bar{2}_{\beta}$ ) and in the direction normal to this two ( $1\bar{1}0_{\beta}$ ). As the formation of the  $\eta$  structure yields a volume increase whereas that of the  $\omega$  structure a volume decrease, the concomitant formation of the  $\omega$  structure is to cancel the volume increase of the  $\eta$  structure and to minimize the lattice distortion of each single formation.

The results of the present work deepen the understanding of the formation mechanism of the two hexagonal structures in the  $B_2$   $\beta$  phase in the Cu-Zn alloys. This is a common feature of the high temperature BCC phase in many other alloys systems, such as Ti alloys and Zr alloys.

### Declaration of Competing Interest

The authors declare that they have no known competing financial interests or personal relationships that could have appeared to influence the work reported in this paper.

### Acknowledgements

The first author Meishuai Liu is grateful to the China Scholarship Council for the support to her study in France. The authors would like to extend their gratitude to the Research Institute of North-eastern University for carrying out TEM examinations, using the JEOL JEM-ARM200F, in this work.

### Funding information

The following fundings are acknowledged: National Nature Science Foundation of China, Grant No. 51471047, the Fundamental Research Funds for the Central Universities No. N130418001, the Science and Technology innovation Action Plan of Shanghai No. 20YF1415700.

### References

- [1] W.G. Burgers, On the process of transition of the cubic-body-centered modification into the hexagonal-close-packed modification of zirconium, *Physica* 1 (7-12) (1934) 561–586, [https://doi.org/10.1016/S0031-8914\(34\)80244-3](https://doi.org/10.1016/S0031-8914(34)80244-3).
- [2] D. De Fontaine, N.E. Paton, J.C. Williams, The omega phase transformation in titanium alloys as an example of displacement controlled reactions, *Acta Metall.* 19 (11) (1971) 1153–1162, [https://doi.org/10.1016/0001-6160\(71\)90047-2](https://doi.org/10.1016/0001-6160(71)90047-2).
- [3] T. Furuhashi, T. Maki, T. Makino, Microstructure control by thermomechanical processing in  $\beta$ -Ti-15-3 alloy, *J. Mater. Process. Tech.* 117 (3) (2001) 318–323, [https://doi.org/10.1016/S0924-0136\(01\)00790-7](https://doi.org/10.1016/S0924-0136(01)00790-7).
- [4] L. Qi, C. Chen, H. Duan, S. He, Y. Hao, H. Ye, R. Yang, K. Du, Reversible displacive transformation with continuous transition interface in a metastable  $\beta$  titanium alloy, *Acta Mater.* 174 (2019) 217–226, <https://doi.org/10.1016/j.actamat.2019.05.045>.
- [5] P. Zhao, C. Shen, M.F. Savage, J. Li, S.R. Niezgoda, M.J. Mills, Y. Wang, Slip transmission assisted by Shockley partials across  $\alpha/\beta$  interfaces in Ti-alloys, *Acta Mater.* 171 (2019) 291–305, <https://doi.org/10.1016/j.actamat.2019.04.013>.
- [6] L. Qi, S. He, C. Chen, B. Jiang, Y. Hao, H. Ye, R. Yang, K. Du, Diffusional-displacive transformation in a metastable  $\beta$  titanium alloy and its strengthening effect, *Acta Mater.* 195 (2020) 151–162, <https://doi.org/10.1016/j.actamat.2020.05.058>.
- [7] H.W. Jeong, Y.S. Yoo, Y.T. Lee, J.K. Park, Elastic softening behavior of Ti-Nb single crystal near martensitic transformation temperature, *J. Appl. Phys.* 108 (2010), <https://doi.org/10.1063/1.3486212> 063515.
- [8] K. Wang, M. Kopec, S. Chang, B. Qu, J. Liu, D.J. Politis, L. Wang, G. Liu, Enhanced formability and forming efficiency for two-phase titanium alloys by Fast light Alloys Stamping Technology (FAST), *Mater. Des.* 194 (2020), <https://doi.org/10.1016/j.matdes.2020.108948> 108948.
- [9] N. Haghdadi, R. DeMott, P.L. Stephenson, X.Z. Liao, S.P. Ringer, S. Primig, Five-parameter characterization of intervariant boundaries in additively manufactured Ti-6Al-4V, *Mater. Des.* 196 (2020), <https://doi.org/10.1016/j.matdes.2020.109177> 109177.
- [10] Y. Gao, Y. Zheng, H. Fraser, Y. Wang, Intrinsic coupling between twinning plasticity and transformation plasticity in metastable  $\beta$  Ti-alloys: A symmetry and pathway analysis, *Acta Mater.* 196 (2020) 488–504, <https://doi.org/10.1016/j.actamat.2020.07.020>.
- [11] H. Guo, P. Liu, X. Qin, Y. Song, D. Qian, L. Xie, L. Wang, L.-C. Zhang, L. Hua, Electroshock treatment dependent microstructural evolution and mechanical properties of near- $\beta$  titanium alloy manufactured by directed energy deposition, *Mater. Des.* 212 (2021), <https://doi.org/10.1016/j.matdes.2021.110286> 110286.
- [12] A. Moridi, E.J. Stewart, A. Wakai, H. Assadi, F. Gartner, M. Guagliano, T. Klassen, M. Dao, Solid-state additive manufacturing of porous Ti-6Al-4V by supersonic impact, *Appl. Mater. Today*. 21 (2020), <https://doi.org/10.1016/j.apmt.2020.100865> 100865.
- [13] X.Q. Jiang, X.G. Fan, M. Zhan, R. Wang, Y.F. Liang, Microstructure dependent strain localization during primary hot working of TA15 titanium alloy: Behavior and mechanism, *Mater. Des.* 203 (2021), <https://doi.org/10.1016/j.matdes.2021.109589> 109589.
- [14] M.J. Lai, C.C. Tasan, J. Zhang, B. Grabowski, L.F. Huang, D. Raabe, Origin of shear induced  $\beta$  to  $\omega$  transition in Ti-Nb-based alloys, *Acta Mater.* 92 (2015) 55–63, <https://doi.org/10.1016/j.actamat.2015.03.040>.
- [15] M. Bönsch, T. Waitz, M. Calin, W. Skrotzki, J. Eckert, Tailoring the Bain strain of martensitic transformations in TiNb alloys by controlling the Nb content, *Int. J. Plasticity*. 85 (2016) 190–202, <https://doi.org/10.1016/j.ijplas.2016.07.010>.
- [16] T. Li, D. Kent, G. Sha, L.T. Stephenson, A.V. Ceguerra, S.P. Ringer, M.S. Dargusch, J.M. Cairney, New insights into the phase transformations to isothermal  $\omega$  and  $\omega$ -assisted  $\alpha$  in near  $\beta$ -Ti alloys, *Acta Mater.* 106 (2016) 353–366, <https://doi.org/10.1016/j.actamat.2015.12.046>.
- [17] Y. Zheng, R.E.A. Williams, S. Nag, R. Banerjee, H.L. Fraser, D. Banerjee, The effect of alloy composition on instabilities in the  $\beta$  phase of titanium alloys, *Scr. Mater.* 116 (2016) 49–52, <https://doi.org/10.1016/j.scriptamat.2016.01.024>.
- [18] J. Fan, J. Li, Y. Zhang, H. Kou, J. Ghanbaj, W. Gan, L. Germain, C. Esling, The origin of striation in the metastable  $\beta$  phase of titanium alloys observed by transmission electron microscopy, *J. Appl. Crystal.* 50 (3) (2017) 795–804, <https://doi.org/10.1107/S1107576717004150>.
- [19] K. Hua, Q. Wan, H. Kou, F. Zhang, Y. Zhang, J. Li, The interplay relationship between phase transformation and deformation behavior during hot compression in a metastable  $\beta$  titanium alloy, *Mater. Des.* 197 (2021), <https://doi.org/10.1016/j.matdes.2020.109275> 109275.
- [20] M.J. Lai, T. Li, D. Raabe,  $\omega$  phase acts as a switch between dislocation channeling and joint twinning-and transformation-induced plasticity in a metastable  $\beta$  titanium alloy, *Acta Mater.* 151 (2018) 67–77, <https://doi.org/10.1016/j.actamat.2018.03.053>.
- [21] D. De Fontaine, Mechanical instabilities in the bcc lattice and the beta to omega phase transformation, *Acta metal.* 18 (2) (1970) 275–279, [https://doi.org/10.1016/0001-6160\(70\)90035-0](https://doi.org/10.1016/0001-6160(70)90035-0).
- [22] S.S. Rao, T.R. Anantharaman, The occurrence of a hexagonal phase in quenched 60: 40 brass, *Sci. Nat.* 48 (1961) 712, <https://doi.org/10.1007/BF00620952>.
- [23] C. Suryanarayana, T.R. Anantharaman, Formation of hexagonal phases in  $\alpha$ - $\beta$  brasses, *Metall. Mater. Trans. B*. 2 (11) (1971) 3237, <https://doi.org/10.1007/BF02814985>.
- [24] A. Prasetyo, F. Reynaud, H. Warlimont, Omega phase in quenched  $\beta$  brass and its relation to elastic anomalies, *Acta Metall.* 24 (11) (1976) 1009–1016, [https://doi.org/10.1016/0001-6160\(76\)90131-0](https://doi.org/10.1016/0001-6160(76)90131-0).
- [25] H.E. Troiani, J.L. Pelegrina, M. Ahlers, The bcc-to-fcc phase transformation during dezincification of  $\beta$ -phase Cu-Zn, *Philos. Mag. A*. 78 (6) (1998) 1253–1267, <https://doi.org/10.1080/01418619808239985>.
- [26] H.E. Troiani, M. Ahlers, The formation of an intermediate structure during the dezincification of  $\beta$  Cu-Zn alloys and its relevance for the martensitic transformation, *Mater. Sci. Eng. A*. 273 (1999) 200–203, [https://doi.org/10.1016/S0921-5093\(99\)00370-6](https://doi.org/10.1016/S0921-5093(99)00370-6).
- [27] H.E. Troiani, A. Tolley, M. Ahlers, High-resolution transmission electron microscopy study of small hexagonal precipitates produced during the dezincification of  $\beta$ -CuZn, *Philos. Mag. A*. 80 (6) (2000) 1379–1391, <https://doi.org/10.1080/01418610008212125>.
- [28] A. Baruj, M. Granada, P. Arneodo Larochette, S. Sommadossi, H.E. Troiani, Primordial hexagonal phase formation during the bcc dezincification of the  $\beta$  Cu-Zn single crystalline surface: Matrix instabilization and transformation path, *J. Alloys Compd.* 481 (1-2) (2009) 129–134, <https://doi.org/10.1016/j.jallcom.2009.02.114>.
- [29] A. Nagasawa, N. Nakanishi, K. Enami, The nature of special-mode softening and the mechanism of martensitic phase transition in  $\beta$ -phase alloys, *Philos. Mag. A*. 43 (6) (1981) 1345–1357, <https://doi.org/10.1080/01418618108239514>.
- [30] Y.Z. Zhou, W. Zhang, J. Guo, G. He, Diffusive phase transformation in a Cu-Zn alloy under rapid heating by electropulsing, *Philos. Mag. Lett.* 84 (5) (2004) 341–348, <https://doi.org/10.1081/09500830410001664535>.
- [31] X.L. Wang, Y.B. Wang, Y.M. Wang, B.Q. Wang, J.D. Guo, Oriented nanotwins induced by electric current pulses in Cu-Zn alloy, *Appl. Phys. Lett.* 91 (2007), <https://doi.org/10.1063/1.2800790> 163112.



- [32] M.S. Liu, Y.D. Zhang, X.L. Wang, B. Beausir, X. Zhao, L. Zuo, C. Esling, Crystal defect associated selection of phase transformation orientation relationships (ORs), *Acta Mater.* 152 (2018) 315–326, <https://doi.org/10.1016/j.actamat.2018.04.031>.
- [33] Y. Zhou, W. Zhang, B. Wang, J. Guo, Ultrafine-grained microstructure in a Cu-Zn alloy produced by electropulsing treatment, *J. Mater. Res.* 18 (8) (2003) 1991–1997, <https://doi.org/10.1557/JMR.2003.0276>.
- [34] B. Beausir, J.-J. Fundenberger Université de Lorraine - Metz, 2017, ATEX - software, Analysis Tools for Electron and X-ray diffraction. [www.atex-software.eu](http://www.atex-software.eu).
- [35] A. Morawiec, J.-J. Fundenberger, E. Bouzy, J.-S. Lecomte, EP—a program for determination of crystallite orientations from TEM Kikuchi and CBED diffraction patterns, *J. Appl. Cryst.* 35 (2) (2002) 287, <https://doi.org/10.1107/S002188980200417X>.
- [36] J.-J. Fundenberger, A. Morawiec, E. Bouzy, J.S. Lecomte, Polycrystal orientation maps from TEM, *Ultramicroscopy* 96 (2) (2003) 127–137, [https://doi.org/10.1016/S0304-3991\(02\)00435-7](https://doi.org/10.1016/S0304-3991(02)00435-7).
- [37] Crystal Maker software, <http://www.crystallmaker.com/>.
- [38] J.J. Jonas, Y.L. He, G. Langelaan, The rotation axes and angles involved in the formation of self-accommodating plates of Widmanstätten ferrite, *Acta Mater.* 72 (2014) 13–21, <https://doi.org/10.1016/j.actamat.2014.03.059>.
- [39] R. Withers, A modulation wave approach to the order hidden in disorder, *IUCrJ.* 2 (2015) 74–84, <https://doi.org/10.1107/S2052252514022556>.
- [40] L.E. Tanner, Diffraction contrast from elastic shear strains due to coherent phases, *Philos. Mag.* 14 (127) (1966) 111–130, <https://doi.org/10.1080/14786436608218994>.